

Blend Electrodes in Lithium-Ion Batteries: Investigation of Inhomogeneities Using a Spatially Resolved Transmission Line Model

Maximilian Schamel, Julian Knorr, Andrea Kinberger, and Michael A. Danzer*

Blend electrodes are used in lithium-ion batteries to increase the performance by combining two active materials, such as silicon (Si) or silicon oxide (SiO_x) and graphite (Gr), for the negative electrode. In-depth knowledge of the complex interactions between the materials is essential to understand how inhomogeneities and local peaks of the intercalation current arise and how they can be prevented. This work presents a spatially resolved transmission line model developed to describe the electrochemical behavior of blend electrodes. Parameterization and model

validation are carried out for a Gr/SiO_x anode. Simulation results are used to investigate inhomogeneities in local states during lithiation at different C-rates. A special focus is put on stress indicators as precursors for accelerated ageing like local material-specific C-rates and spatial gradients of the degree of lithiation. Thus, the modeling approach is a tool for both the description of the properties of blend electrodes and for simulation-based balancing of the active materials' capacities within blend electrodes.

1. Introduction

Lithium-ion batteries (LIBs) are a key technology for efficiently storing and delivering electrical energy across a wide range of applications, including portable electronics, electric vehicles, stationary energy storage applications, and air- and space crafts.^[1–5] Ongoing research aims at further improving their performance, particularly in terms of increasing energy and power density, lifetime, and fast-charging capability. One promising approach is the concept of blend electrodes, also referred to as blended or composite electrodes, where two or more lithium insertion materials are combined to leverage their benefits and achieve synergy effects. This concept can be applied to both cathodes and anodes and is widely used in commercial cells, enabling significant improvements in energy density, power density, and cycling stability.^[6–8] Optimizing the blend composition allows for tailoring the electrode's properties to specific performance

requirements and presents a flexible and effective strategy for advancing energy storage solutions. Recent research has demonstrated that lithium manganese oxide (LMO), which offers good rate capability but low cycling stability,^[6,8] in combination with either lithium nickel cobalt aluminum oxide (NCA), exhibiting high cycle life performance, or with lithium nickel manganese cobalt oxide (NMC), noted for high specific capacity, is a beneficial strategy at the cathode side.^[6,9,10] For the negative electrode, incorporating silicon (Si) or silicon oxide (SiO_x) into the widely used graphite (Gr) anode is a widely adopted strategy.^[11–14] This approach increases the energy density, attributed to the high theoretical capacity of Si and SiO_x. However, in contrast to the comparatively stable Gr electrodes, pure Si or SiO_x electrodes face challenges with poor cycling stability. This is due to the large volume expansion during lithiation, which increases the risk of pulverization, loss of electrical contact, and the formation of additional solid-electrolyte interphase (SEI).^[11,15–18]

Despite the advanced commercialization of blend electrodes, the complex interactions between the materials and the impact of blended designs on internal electrochemical processes remain poorly understood and development is still largely empirical. Operando metrological studies of relevant internal states, such as local degree of lithiation (DOL) and local current densities, are challenging and scarce.^[6,19,20] Since inhomogeneities inside the electrode and high peak intercalation currents can accelerate material degradation, a deeper understanding of the lithiation and delithiation processes is crucial for further advancement. To address these issues, several models have been developed to reveal the internal electrochemical or mechanical behavior of blend electrodes.

A common approach in the literature is to modify the widely used Doyle–Fuller–Newman (DFN) physics-based model^[21–23] to account for two particles representing two different materials at each node.^[24–29] Several works have investigated Gr/Si blend

M. Schamel, J. Knorr, A. Kinberger, M. A. Danzer

Chair of Electrical Energy Systems (EES)

University of Bayreuth

95447 Bayreuth, Germany

E-mail: danzer@uni-bayreuth.de

M. Schamel, A. Kinberger, M. A. Danzer

Bavarian Center for Battery Technology (BayBatt)

University of Bayreuth

95447 Bayreuth, Germany

J. Knorr

BMW Group

Research and Technology Centre

85748 Garching, Germany



Supporting information for this article is available on the WWW under <https://doi.org/10.1002/batt.202500147>



© 2025 The Author(s). *Batteries & Supercaps* published by Wiley-VCH GmbH. This is an open access article under the terms of the Creative Commons Attribution License, which permits use, distribution and reproduction in any medium, provided the original work is properly cited.

anodes with different focuses, such as the influence of mechanics on the electrochemical performance, the development of fast charging strategies, the electrochemical interactions between Si and Gr as well as the nonuniform interfacial current densities across the electrode, or the effect of different mass fractions of Si.^[25–28] Further adaptions of the DFN model considered particles of different radii, film-, and contact resistances,^[30] or coupling it with degradation models to simulate the degradation behavior during cycling under various operating conditions.^[31]

Zhang et al.^[32] developed a porosity model to account for volume changes in active materials and electrode dimensions for Si-based anodes. Liang and Bazant^[33] introduced a mathematical modeling framework for hybrid multiphase porous electrode theory based on the porous electrode theory as used in the DFN model. This model accounts for parallel reactions, phase transformations, and multiscale heterogeneities in blended porous electrodes. Boveleth et al.^[34] published a parameter study to systematically analyze the influence of lithium plating in blend electrodes. A 3D model of the microstructure consisting of two equally sized spherical particles for Si and Gr was used to investigate the relevant parameters affecting lithium plating, and ultimately, the design of blend electrodes.

In the context of blend cathode models, Kespe et al.^[9] studied the interactions between LMO and NMC using a 3D electrochemical model, considering variations in particle size. By virtually altering the proportions of the two materials, they investigated the effects of blend electrode design on, for example, the total usable capacity, local ionic current densities, and the distribution of current between the materials. They found that adding LMO to NMC helps to reduce the maximum lithium concentration gradients in the NMC species during operation, which is considered to decrease degradation due to the minor volume expansion stress in case of lower concentration inhomogeneities inside the particles.^[9]

The literature review shows a trend to study blend electrodes by the use of physics-based DFN or 3D resolved electrochemical models and modifying them to account for two different active materials, usually represented by two parallel particles. However, a large number of parameters needs to be determined for these kinds of models, involving various experimental characterization techniques.^[35,36] Furthermore, solving the partial differential equations describing these models requires high computational effort.

In contrast, Beck and Dubarry^[37] proposed a simplified blend electrode model as an advancement of the mechanistic modeling approach,^[38] which facilitates easier parameterization and is primarily based on the individual voltage response curves of the materials. Their work is focused on the degradation of blend electrodes and their individual components, emphasizing the influence of various degradation modes on current distribution and cell voltage.^[37]

This work introduces a time-domain simulation approach for blend electrodes using a spatially resolved transmission line model (TLM). Costard previously presented this concept in the frequency domain to model impedance spectra of blend cathodes.^[39] In the TLM, equivalent circuit (EC) elements depict the kinetic properties in a porous electrode,^[40–43] which is a commonly used technique to analyze and model impedance spectra.

For example, fitting the parameters of a suitable TLM structure to measurement data is employed for characterizing tortuosity,^[40] active material utilization ratio,^[44] exchange current density,^[45] dendritic growth on metal anodes,^[46] as well as electronic and ionic conductivity in all-solid-state electrodes.^[47,48] Conversely to the frequency domain TLM, the utilization of this model type in the time domain is less common. The spatial resolution of the TLM comes from the division of a defined dimension, such as the thickness of a porous electrode, into a defined number of compartments and their mapping as a dynamic network.

In the time domain, a system of differential-algebraic equations (DAEs) can be set up using a state-space representation to describe the charge transport within the porous electrode structure.^[49,50] Advantageously, parameterization involves only electrochemical impedance spectroscopy (EIS) and open-circuit potential (OCP) measurements.

The parameters of the model are identifiable, which represents a significant advantage over physics-based models that involve a larger set of parameters, many of which are difficult to quantify unambiguously while maintaining physical interpretability. Tackling that issue, Plett and Trimble proposed an approach for physics-based models that incorporates lumped parameter values by mathematically condensing multiple physical parameters that are not independently identifiable.^[51] In comparison, the TLM can be regarded as a more abstracted model that offers real-time capability and a manageable computational effort, as it does not contain partial differential equations. As a result, it provides an efficient alternative to physics-based models, which, in contrast, provide advantages in terms of the accuracy of representing the underlying physical processes. For example, the TLM does not capture local Li concentration and its influence on electrolyte properties, unlike physics-based models.^[22,36,52]

In this work, for the first time to the best of our knowledge, an existing time-domain TLM is extended to account for two active materials in the electrode, thus, a blend electrode. After validation, the model is used to investigate internal states in the electrode and inside the particles during operation.

In particular, stress indicators, such as peak local current rates (C-rates), the inhomogeneity of the DOL, and predicted volume expansion, are examined at different C-rates. These indicators will be used in future works for investigating the degradation behavior, and thus, predicting long-term performance. The aim of this article is to demonstrate blend electrodes and respective operating strategies must be optimized, with a particular focus on the stress indicators, to avoid critical states, and thus, ensure safe operation and an extended service life.

The article is organized as follows: Section 2 describes the modeling approach, that is, the extension of the standard TLM for blend electrodes and the corresponding parameterization procedure. The results of the simulations are presented and discussed in Section 3, starting with a comparison of simulation results and experimental measurements in Section 3.1. Therefore, the measurements from a previous work of Knorr et al.^[53] with an experimental Gr/SiO_x blend setup consisting of two pure half-cells connected in parallel are used. In Section 3.2, local states, inhomogeneities, and possible stress indicators during operation at different C-rates are investigated. To emphasize the impact

of the blend electrode design, a comparison with a pure Gr electrode is made with a focus on peak local C-rates and the resulting DOL inhomogeneities. In Section 4, the key findings are summarized, and a brief outlook on future research directions is given.

2. Modeling Approach

The discrete electrode model used in this study was developed by Hahn et al.^[49,50] in both frequency and time domain for simulating the electrode's impedance and the terminal voltage during operation, respectively. The time-domain model is now modified to simulate a blend electrode. The original model can be applied to simulate porous electrodes that contain one active storage material (AM) with spatial resolution on electrode and particle levels. Similar to the well-known DFN,^[21–23] this can be considered as a pseudo-2D approach (p2D), allowing for the investigation of local states inside the electrode perpendicular to the current collector and inside particles radial from surface to center. In the following, the basic structure and the modification to a blend electrode model are explained. Additionally, the chosen approach for parameterization is examined.

2.1. Transmission Line Model in Time Domain

In contrast to physical DFN models, the TLM is an EC model with spatial resolution. Processes are modeled by distributed electrical EC elements (resistors R , capacitors C , voltage sources U_{OCP}), allowing for the description of the kinetic and thermodynamic properties of the electrode. The included processes are ionic transport in the electrolyte domain, transport across the SEI, charge transfer (CT) at the double layer at the interface between liquid electrolyte and solid AM, solid diffusion inside the AM, and the OCP of the AM. Since the electronic conductivity in the AM in graphite-based anodes is considered to be significantly higher than the ionic conductivity in the electrolyte,^[49] the resistance of the electrical path is neglected. SEI and CT are modeled by two resistive-capacitive (RC) elements while ohmic resistors model ionic transport and solid diffusion.

The model equations are described using a state-space representation and solved iteratively via the linear-implicit Euler method. Fundamental electrical engineering principles, specifically Kirchhoff's current and voltage laws, are employed to derive a set of DAEs.

$$M\dot{x} = f(x, u) \quad (1)$$

with the mass matrix M and the state vector \dot{x} . The state variables consist of the dynamic voltages at all RC elements, the ionic currents in each discrete segment, the solid-state current in each particle shell, and the charge stored in every discrete particle shell. The system function f is defined as

$$f(x) = A(x)x + b(x)u + v(x) \quad (2)$$

Here, $A(x)$ denotes the system matrix, which accounts for the dependency of model parameters on the DOL. b is the input

vector and is multiplied by the input variable u , which represents the applied current I_0 . The nonlinear contributions, $v(x)$, correspond to the DOL-dependent OCPs in the particle shells.

For more details on the model structure and the formulated state equations, the reader is referred to the Supporting Information (Section SI.1) as well as to the previous publications of Hahn et al.^[49,50] which established the model in its basic form, describing a porous electrode with one active storage material.

2.2. Modification towards Blend Electrodes

As a modification of the standard TLM that can be used for electrodes including one AM species, the further developed blend TLM is composed of two separate interfacial paths between liquid and solid domain in every electrode segment i . To the best of our knowledge, this approach was reported first by Costard^[39] with the aim to model the impedance of blend electrodes in frequency domain by a TLM. Furthermore, based on the same assumptions of two parallel AM species existing in every electrode segment, Ai et al. presented a DFN model for blend electrodes.^[27] We now transfer this approach to the time-domain TLM.

The general model structure is shown in Figure 1a, which illustrates a blend anode composed of graphite (Gr) and silicon oxide (SiOx). The particle model is visualized in Figure 1b, representing the second spatial dimension radially from particle surface to center. From here on, it must be distinguished between electrode segments and interfacial paths, since each segment represents one discrete volume element including two interfacial paths, one for each material k . It is assumed that both interfacial paths are connected at the same position along the dimension perpendicular to the separator, which is partitioned into n segments. In each path, the kinetic limitations at the interface defined by SEI and CT are taken into account by two serial RC elements, condensed to $Z_{int,k,i}$ in Figure 1a for simplification. In addition, the particle model is included within each path, considering the solid-state diffusion resistance inside the particles ($R_{diff,i}$) as well as the DOL-dependent OCP $U_{OCP,j}$, both included in every particle shell j (cf. Figure 1b). The particle model determines the effective potential of the particle $U_{k,particle,i}$ along each pathway.

As output variable of the DAE system, we define the terminal voltage of the electrode $U_{Electrode}$, while I_0 is the input variable. $U_{Electrode}$ can be determined via Equation (3) at every time step after solving the DAEs. Therefore, Kirchhoff's voltage law can be applied, for example, along the first Gr pathway near the separator.

$$U_{Electrode} = -I_0R_0 + U_{Gr,SEI,1} + U_{Gr,CT,1} + U_{Gr,particle,1} \quad (3)$$

Both active material species are assumed to be distributed perfectly homogeneously over the electrode thickness. Therefore, in every discrete electrode element, the ions can de-/intercalate in both species. No ionic resistance is assumed between the two materials in the same electrode segment. From a physical perspective, this means that the length of the ionic transport path from the separator to the particle surface is equal in one electrode segment, no matter which material is considered. In contrast, ionic resistance separates two adjacent electrode segments,

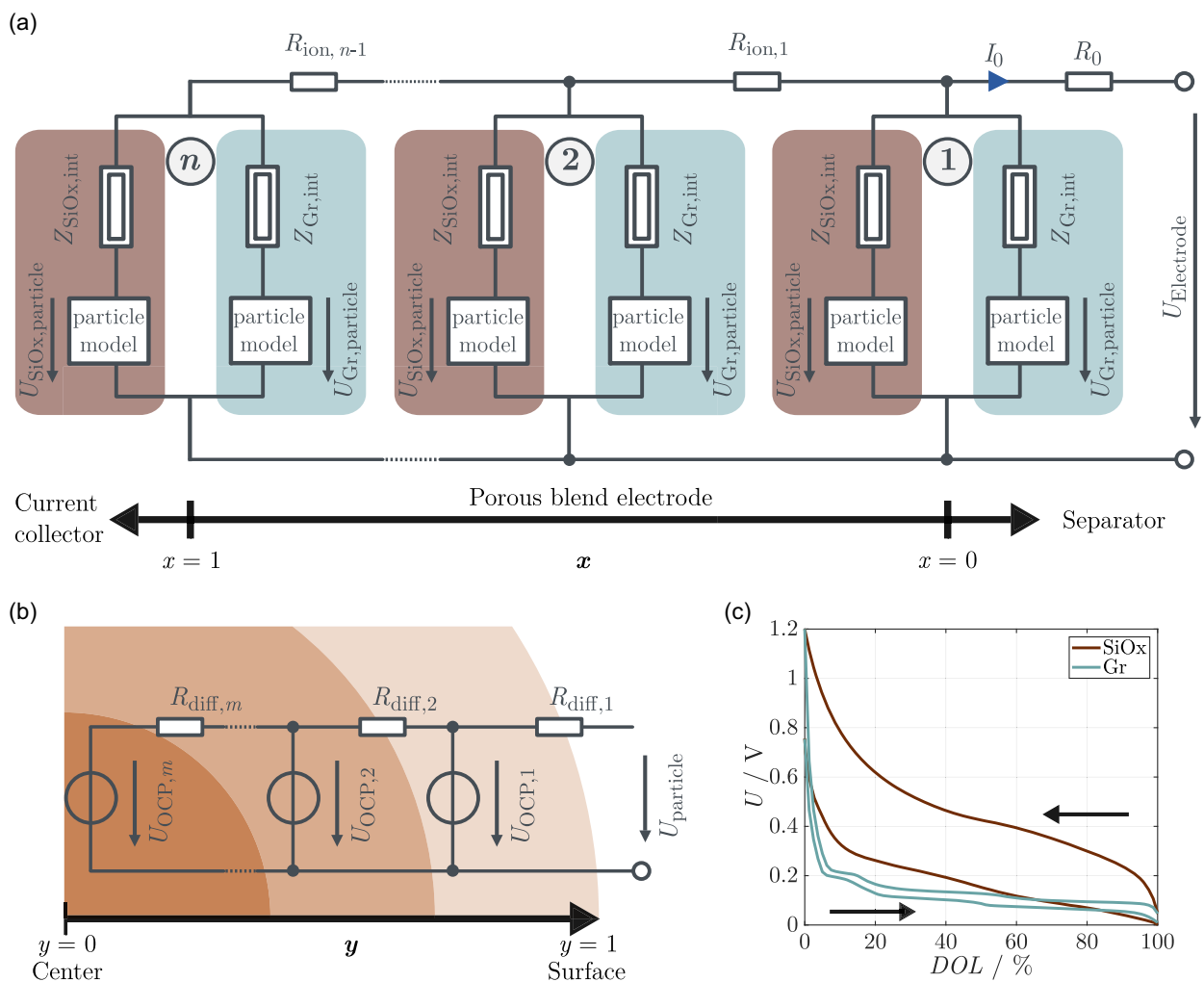


Figure 1. a) Schematic representation of the blend TLM structure for a SiO_x/Gr anode, illustrating spatial resolution along the x-dimension from the separator interface to the current collector interface. b) Particle model with radial discretization along the y-dimension from the surface to the center, assuming spherical particle geometry. c) OCP curves of SiO_x and Gr in dependency of the DOL, showing distinct profiles for lithiation (lower curve) and delithiation (upper curve).

representing the difference in ionic path length. This approach offers the benefit of modeling the current split between the two species in every electrode segment, hence, spatially resolved from separator to current collector.

To account for the material-specific kinetic and thermodynamic properties, two parameter sets are needed for parameterization. All kinetic parameters at the interface between solid and liquid and the OCP curves are material-dependent, indicated by the indices SiO_x and Gr in Figure 1a, representing the species of silicon oxide and graphite, respectively. In contrast, R_{ion} and R_0 do not depend on the AM species.

Since SiO_x shows a significant voltage hysteresis, this needs to be considered in the blend electrode model as a further development of the original TLM, in which this phenomenon was neglected so far when pure Gr electrodes were modeled.

Although multiple models for the voltage hysteresis of LIB electrodes have been presented,^[54–57] including mechanistic, phenomenological, and physically motivated EC approaches, a universal solution has not been found yet. In particular, the hysteresis characteristics of Si-containing electrodes are not trivial to

describe and present a major challenge in current research,^[58,59] but this is not the focus of this work. Therefore, we decided for a hysteresis approach according to the well-known one-state model of Plett,^[54] since it is comparably easy to implement in the TLM structure. Thus, one additional hysteresis state h_{ij} is implemented in each discrete particle shell that determines whether the lithiation or the delithiation curve of the OCP is applicable. h ranges between -1 (lithiation) and +1 (delithiation) with a smooth transition in between, depending on the intercalation current direction applied to the considered particle shell. The applied OCP curves are displayed in Figure 1c for SiO_x and Gr, with the lower curve relating to lithiation and the upper curve relating to delithiation. Further details on the hysteresis approach are provided in the Supporting Information (Section SI.2).

2.3. Parameterization

The kinetic parameters of the TLM (R , C) can be determined by impedance fitting. Therefore, the parameters of the frequency

domain TLM are fitted to EIS measurements at different DOLs. This results in values R_{eff} and C_{eff} describing the effective polarization of the considered electrode. Based on that, the calculation of the local parameters for each electrode segment and particle shell is conducted based on the number of discrete electrode segments $n \in N$ and particle shells $m \in N$. For example, the global ionic resistance R_{ion} is uniformly distributed across all n segments, leading to a local value in segment i given by $R_{\text{ion},i} = R_{\text{ion,eff}}/n$, as the ionic resistors appear in series in the TLM structure (cf. Figure 1a). Conversely, the local values of resistors arranged in parallel along the interfacial paths (R_{CT} , R_{SEI}) are calculated following the basic rules of electrical network theory, that is, $R_{x,i} = R_{x,\text{eff}} \cdot n$, with $x \in \{\text{CT, SEI}\}$.

The nominal storage capacity in each particle shell, denoted as $C_{N,i,j}$, is allocated based on the volume fraction of the respective element, ensuring that the sum of the capacities across all particles equals the total electrode capacity C_N . C_N can be parameterized by a standard capacity measurement.

Lastly, the OCP curves of the active materials are needed to describe the local charge-dependent potential $U_{\text{OCP},i,j}(\text{DOL}_{ij})$ in every particle shell in every electrode segment. The local DOL is defined via

$$\text{DOL}_{ij} = \frac{Q_{ij}}{C_{N,i,j}} \quad (4)$$

where Q_{ij} denotes the charge amount that is stored in the considered particle shell.

To parameterize the Gr/SiO_x blend anode considered in this work, we use the data sets of two separate pure electrodes (Gr and SiO_x) that were measured in a setup with Li metal as counter electrode. Both electrodes were characterized by applying EIS at different DOLs and performing pseudo-OCP measurements at a current rate of C/40. The electrode properties are described in detail in the work of Knorr et al.^[53]

The nominal capacities of the AM species were aligned with those determined in the experimental study (cf. Section 3.1), amounting to 2.2 mAh for SiO_x and 6.2 mAh for Gr, which correspond to relative capacity proportions of 26% and 74%, respectively, and a total blend electrode capacity of 8.4 mAh.

To determine the material-specific kinetic parameters at the solid–liquid interface and inside the particles, a 0D EC model (ECM) of the structure $R_0-(RC)_1-(RC)_2-\text{FSW}$ is fitted to the EIS data at five distinct DOLs. The SEI and CT parameters are extracted from the RC elements $(RC)_1$ and $(RC)_2$ while R_{diff} represents the resistance of the finite-space Warburg element (FSW) of the 0D ECM. To complete the kinetic parameter set of the blend TLM, one global effective R_{ion} in the blend and one global R_0 are needed. Since the pure SiO_x and Gr electrodes employed for parameterization exhibit strongly diverging properties in terms of electrode thickness and porosity, it is expected that the ionic resistance in a blend electrode is not comparable to the pure electrodes. Therefore, in this work, R_{ion} is determined by fitting the blend TLM to the time-domain measurement of the model-like blend setup constructed of the two pure electrodes. Details on the measurement setup are provided in Section 3.1. Since it is assumed that the volume expansion of

Table 1. Overview of how the different parameters for the blend TLM are determined. Distinction between material-specific (m) and global blend (b) parameters.

Parameter	Scale	Origin
Voltage curve $U_{\text{OCP},k}$	m	Pseudo-OCP C/40 (pure electrodes)
Capacity $C_{N,k}$	m	Capacity measurement (pure electrodes)
Interfacial path kinetics (R_{CT} , R_{SEI} , R_{diff} , C_{CT} , C_{SEI})	m	ECM fit (pure electrodes)
R_{ion}	b	Fit to time-domain measurement (C/10 lithiation) of blend setup
R_0	b	Assumption: mean R_0 value from ECM fit of both materials

SiO_x significantly influences the porosity, and hence, the ionic transport properties in a blend electrode,^[25,53] for simplification, we assume a linear dependency between the DOL of the SiO_x species in each electrode segment and the corresponding $R_{\text{ion},i}$. For parameterization, the mean value of R_{ion} across the full DOL range is fitted to the measurement data of a C/10 lithiation process. More details on the measurements used for parameterization and validation are given in the Table S1, Supporting Information, and the trend of the fitted kinetic parameters versus DOL can be found in Figure S1, Supporting Information. Table 1 summarizes the parameterization procedure for all parameters. The validation of the acquired parameter set is provided in Section 3.1.

As a peculiarity of the blend TLM in comparison to the standard TLM, the local kinetic parameters in every discrete electrode segment are calculated with regard to the number of segments n , which is half the number of interfacial paths since two materials are contained.

The presented approach—utilizing experimental data from two separate pure electrodes to parameterize the individual species in a blend electrode—offers a pragmatic solution to the challenge of identifying material-specific parameters in blend electrodes. To the best of our knowledge, no existing methodology or experimental design currently enables the independent identification of kinetic parameters for the individual materials within a real blend electrode. This approach inevitably involves certain limitations, for example, transport limitations between the two active materials may differ from those observed in the pure electrodes. Nevertheless, it is considered a reasonable and effective first step toward disentangling the individual contributions of the two AM species in a blend electrode TLM.

3. Results and Discussion

In the following, the results of the blend electrode TLM simulations are validated. Moreover, local states and inhomogeneities during operation are investigated and discussed, thus, highlighting the benefits of the spatially resolved model structure.

3.1. Comparison of Simulation and Measurement at Different C-Rates

Since direct measurements of the internal current split between two active material species in a blend electrode are not feasible, validating the implemented model presents a substantial challenge. To address this, we utilize experimental data from the previous study by Knorr et al.^[53] where the two active materials, silicon oxide and graphite, were separated in two pure-material half-cells, each with a Li metal counter electrode. The cells were assembled in T-cell setup with a diameter of 12.7 mm. These individual half-cells were connected in parallel to form a model-like blend setup, enabling the investigation of the current split between the Gr|Li and SiO_x|Li cells during operation and relaxation. The experimental method was originally developed by Heubner et al.^[6,60] and Liebmann et al.^[61]

The half-cells in the blend setup are equivalent to those employed for the parameterization of the model (cf. Section 2.3).

In the study conducted by Knorr et al.^[53] the lithiation behavior of the blend setup was examined across a range of C-rates, from C/40 to 1C, focusing on the influence on the material-specific DOLs reached in the Gr and the SiO_x fractions during lithiation. By customizing the coating thickness and the proportions of binder and additives of the two electrodes, a SiO_x weight fraction of 8.5% relative to the total electrode weight (sum of Gr and SiO_x electrodes) was achieved. This target was selected to build a blend setup aligned with the range of SiO_x content typically found in commercial cells. The measured reversible capacities of the SiO_x and Gr half-cells at C/40 were 2.2 and 6.2 mAh, respectively. Therefore, the capacity proportion of the SiO_x fraction on the measured total capacity was 26%. The applied C-rate in the experiments was calculated based on the total blend capacity, C_N , which is defined as the sum of the capacities of

the SiO_x and Gr half-cells, C_{N,SiO_x} and $C_{N,Gr}$, respectively. For a comprehensive description of the experimental setup, material properties, and cell assembly, readers are encouraged to consult the original study.^[53] Although the blend setup does not perfectly replicate the conditions of a real blend electrode, where particles of the two active materials are in direct contact within a single electrode, the primary effects arising from the thermodynamic and kinetic properties of the materials are assumed to be comparable. In the following, the TLM simulation results of lithiation processes at different C-rates are compared with the measurements.

Figure 2 presents the blend electrode terminal voltage $U_{\text{Electrode}}$ for C/20, C/10, and C/3 (a–c) alongside the corresponding current split to the SiO_x and Gr material fractions I_{Material} (d–f) versus $DOL_{\text{Electrode}}$. From the model output, the cumulative current for all n discrete electrode segments of SiO_x and Gr is calculated to determine the total intercalation current supplied to each material. Furthermore, the corresponding plots for C/40 and 1C lithiation are presented in the Figure S2, Supporting Information, along with the course of the deviation between U_{Sim} and U_{Meas} . For all investigated C-rates, the major part of the applied current is initially supplied to the SiO_x fraction, while the contribution of Gr remains relatively minor (cf. Figure 2). This trend reverses at $\approx 20\%$ $DOL_{\text{Electrode}}$, where the current of the Gr fraction exceeds the current of the SiO_x fraction. Beyond this point, Gr dominates the intercalation process. At C/20 and C/10, an undulating pattern in I_{Material} is observed in both the measurement and the simulation during this phase. The behavior across the DOL range can be attributed primarily to the interaction between the differing OCP curves of the two species and the kinetic characteristics. For a detailed discussion of the interplay between Gr and SiO_x in general, readers are directed to the experimental paper.^[53]

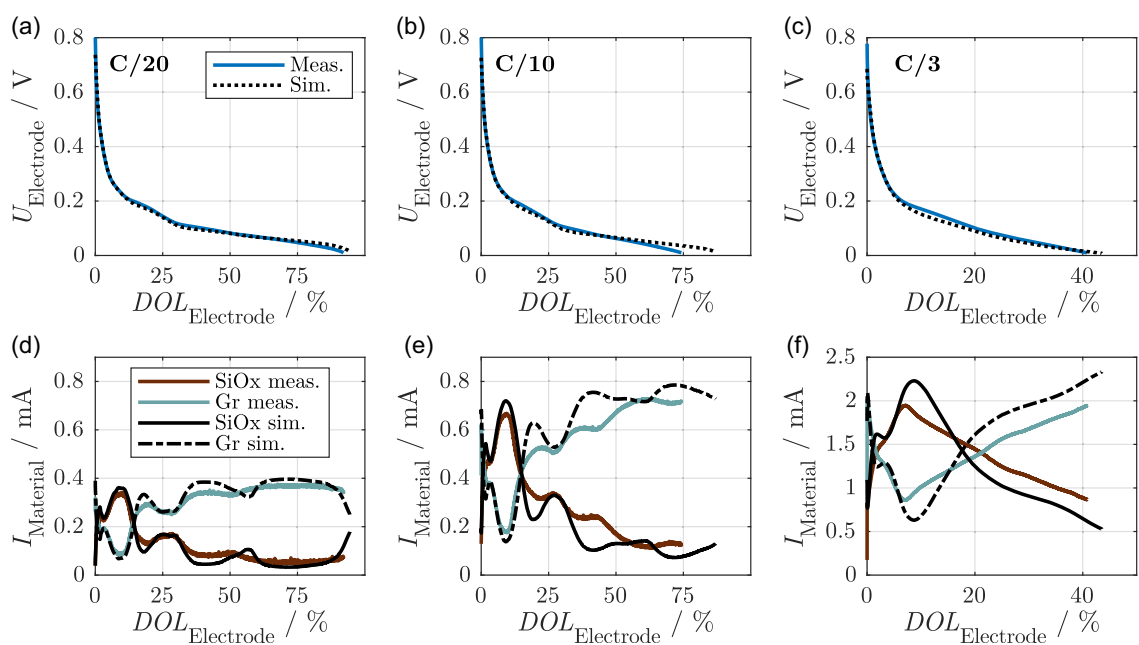


Figure 2. Lithiation process of the blend electrode with $U_{\text{Cutoff}} = 10$ mV at three different C-rates: Comparison of measurement and simulation. Terminal voltage in a–c) and corresponding current split between the two species in d–f) for C/20, C/10, and C/3, respectively.

The comparison in Figure 2 illustrates that the model is capable of qualitatively reproducing the electrochemical behavior of the blend electrode. However, discrepancies between the simulated and the measured values are evident, as the simulated Gr current is higher than the experimental values at medium $DOL_{\text{Electrode}}$, and the oscillations are more pronounced (cf. Figure 2d,e). At C/3, the region with an undulating current split is not reached, as the lithiation process is terminated at 10 mV. The qualitative agreement between the measurement and the simulation in the accessible DOL range is high for this case, although the absolute current values differ slightly, showing a systematical overestimation of the contribution of the species with the higher current (cf. Figure 2f).

Examining the terminal voltage in Figure 2a–c, the largest deviations occur at the beginning of the lithiation process, as confirmed by the analysis of the absolute deviation (cf. Figure S3, Supporting Information). U_{Meas} is significantly higher than U_{Sim} immediately after the current is applied. At C/20 and C/10, another region with substantial deviations arises toward the end of the process. In contrast to the beginning, U_{Meas} is observed to be lower than U_{Sim} , as shown in Figure 2a,b. This leads to a higher charge throughput, and consequently, a higher $DOL_{\text{Electrode}}$ in the simulation until U_{Cutoff} is reached. At C/3, this effect is less pronounced, but the same trend is observed.

Despite this work focusing on effects during lithiation, the results of a full cycle with C/20 lithiation followed by C/40 delithiation are provided in the Supporting Information (Figure S4), including the material-specific DOLs during the whole cycle. The results indicate that the blend TLM is also capable of reproducing the main phenomena during delithiation. The different C-rates of lithiation and delithiation result from the fact that the lithiation at different C-rates in the experimental work^[53] was always followed by standard delithiation at C/40. Therefore, up to this point, experimental data on delithiation at different C-rates of the investigated blend setup is lacking.

To explicitly analyze the attainable charge throughput during lithiation, Q_{lith} , the total charge amount in the blend electrode and in the two materials are shown in Figure 3 for all considered C-rates. The primary trend found in the experimental study is that

the reduction in usable electrode capacity at elevated C-rates is primarily attributed to a decline in Gr charge throughput, whereas, the SiOx charge throughput exhibits only a modest decline up to C/3.^[53] At 1C, however, the SiOx decrease is pronounced. The simulation results indicate that the model generally reproduces this effect, particularly with regard to the usable SiOx capacity, where there is a high congruence for C-rates of up to C/3. Conversely, notable discrepancies are evident in the Gr and the blend charge throughput at C/20 and C/10, where the simulation results exceed those of the measurements. At 1C, both the SiOx and the Gr charge amounts are observed to be lower in the simulation than in the measurement.

A possible explanation for the differing deviations at low and medium C-rates, as opposed to high C-rates, may lie in the absence of current-dependent kinetic parameters in the TLM. Unlike physical DFN models, the TLM does not incorporate Butler–Volmer kinetics for the CT process. Instead, the CT overpotential is modeled by RC elements with constant parameters, irrespective of the applied current.

This model approach may result in underestimating the overpotential at low C-rates and overestimating it at higher C-rates. As a consequence, the charge throughput before reaching U_{Cutoff} deviates from the experimental measurements. Given that Gr becomes more active at higher $DOL_{\text{Electrode}}$, this discrepancy particularly impacts the Gr capacity throughput.

Another notable feature is the deviation in the current split within the range where Gr dominates the lithiation process ($DOL_{\text{Electrode}} > 20\%$), particularly at C/10 and C/20. This suggests that tuning the material-specific parameters could improve the fit between the simulation and the experimental data since the current split is governed by the relation of the OCPs and the kinetic resistances of the two species.

Nonetheless, the parameter sets used allow a qualitative reproduction of the primary effects observed in the blend setup measurements, which is the objective of this work. Refining the parameterization process and addressing the deviations in detail, for example, through a comprehensive analysis of parameter sensitivities, will be the focus of future work.

3.2. Local States and Inhomogeneities during Operation

Due to power constraints arising from electronic and ionic resistances, the capability of LIBs to store and deliver current reversibly may be exceeded during operation. This places the battery under stress. Borrowing from the biological definition of stress,^[62] stress in a battery context refers to a scenario where operational or environmental demands surpass the battery's rate capability. In addition to operating at high C-rates, staying close to the voltage limits or at extreme temperatures can also be a source of stress. Prolonged stress over extended periods of time can trigger degradation mechanisms, accelerate ageing, and damage the cells. Therefore, identifying the early signs of stress in the battery is crucial for maintaining its performance and longevity. Such indicators can be inhomogeneous conditions in the cell,^[63] as the limited performance of mass transport and kinetic capabilities puts different areas under different loads. Further stress

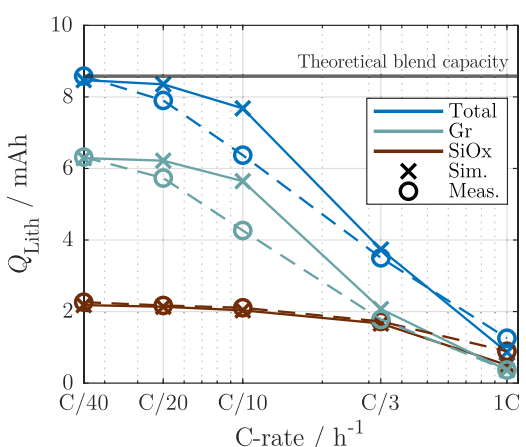


Figure 3. Contributions of SiOx and Gr to total utilizable electrode capacity during lithiation at different C-rates. Comparison between measurement^[53] (o) and simulation (x). The solid and dotted lines serve as a guide for the eye.

indicators can be the occurrence of locally different reaction rates, locally different potentials,^[63] which can result in temperature and expansion gradients across the cell. In the following, inhomogeneous states occurring under operation are examined on the basis of local material-specific current rates, local DOL, and volume expansion. Therefore, different global C-rates are analyzed, ranging from C/40 to 1C.

3.2.1. Local Material-Specific C-Rates

In order to obtain a more accurate assessment of the current distribution between the two AM species, it is helpful to normalize the intercalation current in each discrete element to its corresponding storage capacity. Thus, the local C-rate is calculated via

$$C\text{-rate}_{\text{local}} = \frac{I_{\text{int},i,k}}{C_{N,i,k}} \quad (5)$$

where $C_{N,i,k}$ is the capacity of AM species k in electrode segment i and $I_{\text{int},i,k}$ indicates the respective intercalation current. As shown in Figure 2d-f, the current split between SiO_x and Gr leads to a high peak current imposed on the SiO_x species during the early phase of lithiation. Since C_{N,SiO_x} is only 26% of the total electrode capacity C_N , the calculated local C-rates are of great interest in the context of material stress. The local C-rates are illustrated for C/10 and C/3 lithiation as representative examples in Figure 4, while

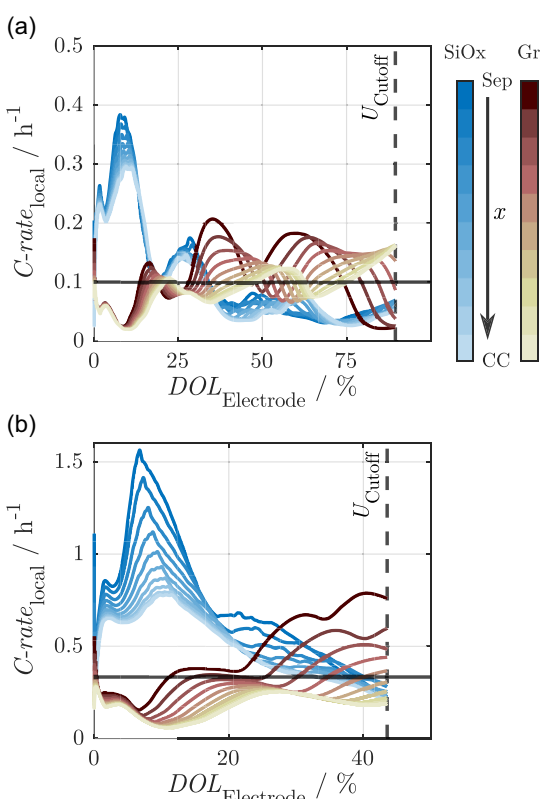


Figure 4. Material-specific C-rate with spatial resolution along the dimension x from separator (dark color) to current collector (light color) during lithiation with a) C/10 and b) C/3. For orientation, the black horizontal line indicates the applied C-rate. The dotted vertical line represents the termination of the lithiation process due to the terminal voltage falling below U_{Cutoff} .

the observed peak values exposed to each material during the lithiation process at five different global C-rates are listed in Table 2. In Figure 4, the local C-rates are presented with spatial resolution from the separator to the current collector, as indicated by the color bar. The different line styles distinguish between the active materials, the black horizontal line refers to the globally applied C-rate. It becomes visible that the local C-rate can strongly differ from the applied global electrode C-rate.

As demonstrated in the work of Hahn et al.^[49] the TLM can be used to study the inhomogeneous current distribution across the electrode thickness during operation due to limited ion transport within the porous electrode. Beyond these spatial inhomogeneities, the coexistence of two AM species in the blend electrode introduces additional inhomogeneity, as the current is unevenly split between the materials. The general trend regarding the split between SiO_x and Gr is consistent across all shown C-rates. The SiO_x species experience a high current during the early stage of lithiation, approximately up to 20% $DOL_{\text{Electrode}}$.

For all C-rates, the peak C-rate observed in the SiO_x species during the whole lithiation process is higher than that in the Gr species, as shown in Table 2. The SiO_x fraction near the separator is exposed to local C-rates more than three times as much as the globally applied C-rate, while the ratio is even increased at higher C-rates, culminating in 5.61C reached locally during 1C lithiation (cf. Table 2). Looking at the spatial inhomogeneities across the electrode thickness, from the separator to the current collector, a significant amplification at higher C-rates can be observed. As shown in Figure 4a, at C/10, the SiO_x peak C-rate of all electrode segments is in the range between 0.3C and 0.38C, whereas at C/3, the range is around 0.7C–1.6C (cf. Figure 4b). The peak C-rates of the Gr fraction as well as the maximum inhomogeneities occur later in the lithiation process, approximately between 30% and 60% $DOL_{\text{Electrode}}$. Given the different operating OCP ranges of the two materials, the current is observed to be higher at medium and high $DOL_{\text{Electrode}}$, where Gr is preferably active after the initial phase of SiO_x lithiation.

Apart from that, the greatest inhomogeneity in Gr, regardless of whether pure or blend electrodes are considered, occurs in the region where the OCP curve shows plateaus and the slope is low.^[49] Similar to SiO_x, the peak C-rates are observed at the separator interface where the ionic pathway is shortest. In contrast to SiO_x, the maximum local C-rates exposed to the Gr fraction are modest and about twice the global C-rate except for 1C lithiation. Here, it has to be considered that at 1C, the achievable $DOL_{\text{Electrode}}$

Table 2. Simulation results: maximum local material-specific C-rates in Gr and SiO_x species during lithiation to $U_{\text{Cutoff}} = 10$ mV at different applied global C-rates.

Global	C-rate in h ⁻¹		$DOL_{\text{Electrode}}$ in %
	Max. SiO _x	Max. Gr	
0.025	0.09	0.05	99
0.05	0.18	0.10	97
0.1	0.38	0.21	90
0.33	1.56	0.79	43
1.0	5.61	1.84	10

in simulation is only 10% due to the cutoff voltage at 10 mV. Therefore, the range where Gr is preferably active and would reach peak C-rates is not covered. Thus, the results of 1C lithiation are not comparable when looking at the maximum Gr C-rates.

In summary, the evaluation of local material-specific C-rates reveals that the coexistence of SiO_x and Gr in a blend electrode leads to significantly higher local C-rates applied to the SiO_x fraction. The lithiation of SiO_x predominantly takes place during the initial stage of electrode lithiation, leading to high current peaks and substantial electrochemical stress on the SiO_x particles. The elevated current initially imposed on the SiO_x must be distributed across the available particles, resulting in a high local load relative to the specific capacity. This is due to the fact that the weight fraction, and consequently, the capacity of SiO_x is lower than that of Gr, which is typical in state-of-the-art commercial cells. At higher C-rates, the effect is further intensified near the separator interface due to increased spatial inhomogeneity.

3.2.2. Inhomogeneity of DOL

Moreover, spatial inhomogeneities of the DOLs within the blend electrode during the simulated lithiation periods are evaluated. Equivalent to the local C-rates in Figure 4, the material-specific local DOL in each electrode segment for C/10 and C/3 lithiation is shown in Figure 5a,b with spatial information given by the color bar. The global electrode DOL is given on the horizontal

axis and indicated by the black angle bisector. For the calculation of the local DOLs displayed, the particles within each electrode segment are treated as homogenized, providing the mean DOL for the entire particle without discretizing from particle surface to center. This allows for an evaluation of the inter-particle inhomogeneity of the DOL, and thus, the deviation of the local DOL across the thickness of the electrode.

As expected, spatial inhomogeneities become more pronounced at higher C-rates in both the SiO_x and the Gr species. Regardless of the global C-rate, particles facing the separator consistently exhibit a higher DOL compared to those near the current collector (CC) throughout the entire process. As demonstrated in the experimental study by Knorr et al.^[53] the SiO_x fraction initially undergoes faster lithiation and exhibits a higher value than the DOL_{Electrode} across all segments. Only at high degrees of lithiation of about 85%, the mean electrode DOL starts to exceed that of the SiO_x segments near the CC, provided that the applied C-rate is low enough to reach the range of DOL_{Electrode} before the terminal voltage is falling below U_{Cutoff}. This is observable at a rate of C/10, as shown in Figure 5a. For the Gr fraction, the DOL near the CC remains consistently lower than the DOL_{Electrode}, while the particles near the separator exceed the DOL_{Electrode} at around 30–40% at both C/10 and C/3. For a detailed evaluation of the occurring inter-particle deviations between separator and CC, the difference between both values, referred to as ΔDOL_{inter} , is calculated separately for the two materials and shown in Figure 6a,b for C/10 and C/3 lithiation, respectively. Interestingly, the SiO_x fraction does not show the largest deviations across the electrode thickness in the early stage of DOL_{Electrode} where the peaks in terms of local C-rates are noticed (cf. Figure 4). Instead,

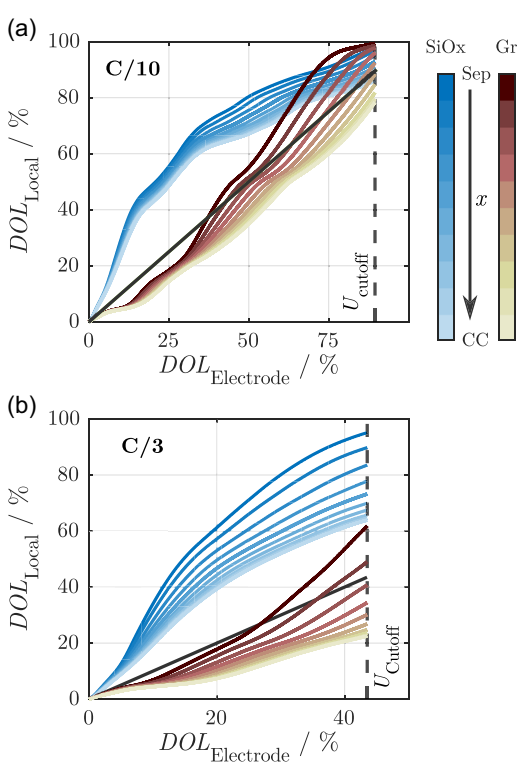


Figure 5. Local DOL with spatial resolution along the dimension x from separator (dark color) to current collector (light color) during lithiation with a) C/10 and b) C/3. The black angle bisector illustrates the mean electrode DOL. The dotted vertical line represents the termination of the lithiation process due to the terminal voltage falling below U_{Cutoff} .

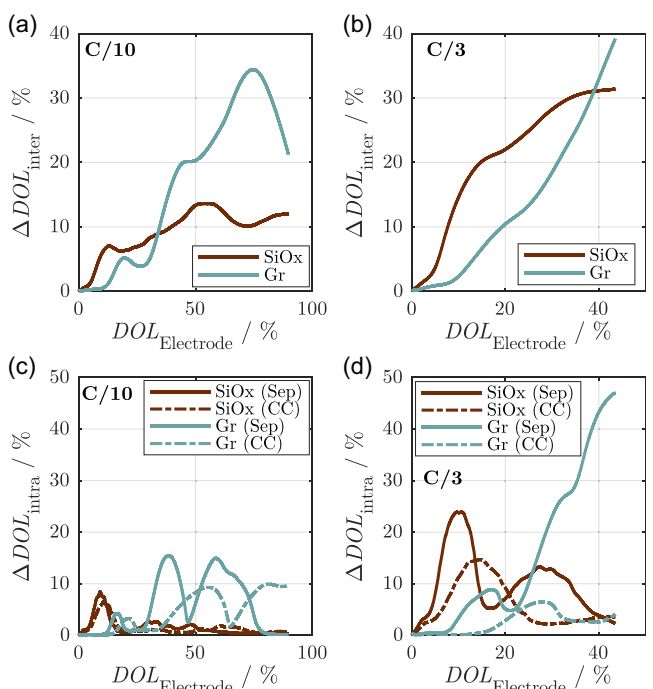


Figure 6. Material-specific DOL inhomogeneity between separator and current collector during lithiation with a) C/10 and b) C/3. Material-specific DOL inhomogeneities between particle surface and center during lithiation with c) C/10 and d) C/3.

at C/10, the maximum $\Delta DOL_{\text{inter}}$ of 14% is detected at 50%–60% $DOL_{\text{Electrode}}$, while at C/3, the peak of 32% $\Delta DOL_{\text{inter}}$ is reached at the moment when the lithiation process is terminated (42% $DOL_{\text{Electrode}}$). This indicates that an even higher inhomogeneity is expected in case the cutoff voltage is different or reached later due to other kinetic parameters. Considering the Gr fraction, an even higher $\Delta DOL_{\text{inter}}$ is detected at medium and high $DOL_{\text{Electrode}}$. At C/10, the greatest inhomogeneity is 34% and occurs at 74% $DOL_{\text{Electrode}}$. At C/3, the difference between separator and CC is further increased and reaches 39% at the end of the lithiation process.

Apart from the inter-particle deviations along the dimension perpendicular to the separator, inhomogeneities also arise within the particles themselves. In the TLM, as second dimension, each particle in the electrode segments is radially discretized from the surface to the center, assuming spherical geometry. This allows for the evaluation of the effects of limited Li^+ solid-state diffusion within the AM. We refer to these diffusion-related effects as intra-particle inhomogeneity, and $\Delta DOL_{\text{intra}}$ is defined as the difference between the DOLs at particle surface and center. Figure 6c,d illustrates $\Delta DOL_{\text{intra}}$ for the C/10 and C/3 lithiation, respectively. For each material, the intra-particle inhomogeneity is evaluated for the separator- and CC-facing particles, since, these represent the extremes across dimension x , hence, along the electrode thickness.

Again, a higher C-rate induces larger inhomogeneity due to kinetic limitations. Contrary to the inter-particle inhomogeneity, the $\Delta DOL_{\text{intra}}$ peak of the SiO_x fraction occurs during the first 20% of lithiation for both depicted C-rates. The peaks of the particle facing the separator are higher compared to the CC and occur at an earlier time. This can be observed for both materials. At C/3, the maximum $\Delta DOL_{\text{intra}}$ of the Gr species is detected at the end of the simulated lithiation and amounts to 47%, compared to 15% at C/10. Looking at the SiO_x fraction, it can be noticed that after the peak is reached in an early stage of the process, the intra-particle inhomogeneity decreases and, for example, at C/10, flattens to almost zero. Thus, the DOL inside the SiO_x particles homogenizes. The Gr fraction shows higher inhomogeneity inside the particle near the CC at the end of C/10 lithiation than near the separator. This underlines that the limited ionic transport across the electrode thickness leads to delayed utilization of the particles near the CC.

It is assumed that the higher maximum DOL inhomogeneities in Gr compared to SiO_x, both inter-particle and intra-particle, are due to the flat regions in the OCP curve of Gr. That allows for a wide distribution of DOL values where the OCP is almost similar, and thus, the driving force for a homogenization of the DOL is low. Apart from that, Gr is active throughout a wider range during electrode lithiation, while SiO_x is active preferably from 0% to around 20% $DOL_{\text{Electrode}}$. That allows the SiO_x species to homogenize while the current is mainly supplied to Gr at medium and high $DOL_{\text{Electrode}}$. When looking at the results, it has to be considered that the emerging inhomogeneities are highly sensitive to the kinetic parameters describing the transport across the electrode and inside the particles, namely R_{ion} and R_{diff} . The parameterization of the model is based on EIS fitting using measurements with a minimum frequency of 100 mHz (cf. Section 2.3).

Thus, the solid-state diffusion characteristics are not covered completely in the measurement, and the fitted parameters $R_{\text{diff},\text{Gr}}$ and $R_{\text{diff},\text{SiO}_x}$ are subject to a high degree of uncertainty. If alternative parameterization approaches yielded different parameter values, the resulting intra-particle inhomogeneities would also differ. Despite this sensitivity, the main trends demonstrated in the simulation would remain similar. However, the absolute values should be interpreted cautiously, as they may not accurately reflect the true extent of DOL inhomogeneities.

The insights gained on 2D DOL inhomogeneity could provide valuable guidance for the further improvement of blend electrode designs. Large DOL gradients from separator to CC inhibit the full utilization of electrode capacity, negatively impacting energy and power density.^[12,64,65] Hence, optimized design approaches or material improvements could enable a more homogenized utilization of the AM particles. This is relevant especially for blend electrodes since the simulation results indicate a highly inhomogeneous lithiation process because of the fluctuating current split between SiO_x and Gr. Additionally, significant intra-particle inhomogeneity of the DOL is believed to accelerate cyclic ageing due to the mechanical stresses generated within particles,^[9,66] as further discussed in Section 3.2.3.

3.2.3. Coupling with Material-Specific Volume Expansion

A key challenge associated with Si and SiO_x in battery electrodes is the significant volume expansion that occurs during lithiation. In general, volume expansion can lead to accelerated degradation due to particle pulverization and loss of contact within the electrode structure.^[17,18,66–68] To address this, the results of the TLM simulations are now used to approximate the expected expansion of the discrete electrode segments and particle shells of the TLM structure. In a first approach, the DOL of the individual particle shells is mapped to the volume expansion by means of a nonparametric model and the operando volume expansion is calculated during the simulated lithiation process. It should be noted that the model approach used here does not account for interactions between electrochemical and mechanical processes, unlike certain studies that employ advanced physics-based models.^[69,70] In this work, volume expansion is calculated in a post-processing step based on the values of DOL_{Local} resulting from the TLM simulations. This analysis focuses solely on the expansion behavior of the SiO_x species since the expansion of Gr is small in comparison.^[71] It is assumed that at a DOL of 100%, a species defined by $x = 3.5$ in Li_xSiO is present. This state is reached during C/40 lithiation to the lower cutoff voltage in the experimental study and used for parameterization.^[53] This corresponds to a maximum relative volume v_{rel} of 220% normalized to the initial volume V_0 in the delithiated state, as calculated by Jung et al.^[72] In between 0% and 100% DOL, a linear increase of v_{rel} is assumed, approximating the findings from literature.^[25,71,72] Therefore, the relative volume of the SiO_x fraction in the blend electrode is described via

$$v_{\text{rel},ij}(DOL_{ij}) = 1 + 1.2 \cdot DOL_{ij} \quad (6)$$

and can be calculated for every time step and every discrete element in electrode segment i and particle shell j based on the

results of the electrochemical simulation. It should be noted that this approach provides only a rough approximation, as the precise chemical composition of the material at 100% DOL remains uncertain. The coexistence of multiple lithiated SiO_x compounds is likely,^[53] each exhibiting different v_{rel} in the fully lithiated state, which may range from 200% to 400%.^[18] Consequently, the absolute values calculated for volume expansion may vary depending on the specific assumptions and the considered voltage range.

Figure 7 illustrates the results for a lithiation process at C/3, thus, a relatively high rate where expansion-induced degradation phenomena are supposed to be more pronounced. To examine inter-particle inhomogeneities, both the relative volume during lithiation of (1) the particle adjacent to the separator and (2) the particle near the CC are analyzed. Intra-particle inhomogeneities are also evaluated by comparing the particle surface shell with the particle center, according to the discretization approach shown in Figure 1b. The results show that the SiO_x particles located near the separator exhibit significantly greater expansion compared to the particles near the current collector, which is due to the higher DOL reached at the separator interface. Furthermore, significant inhomogeneity is observed within the particles at both the separator and the current collector interfaces, although a homogenization can be observed at the end. The particle facing the separator shows slightly higher inhomogeneity during the process in comparison to the particle near the CC. Large expansion variations inside the particles could be a hint for accelerated particle cracking, and hence, should be prevented. Due to the high local C-rates of up to 1.6C in the SiO_x species near the separator at the considered rate (cf. Figure 4), the inhomogeneities are enhanced and the particles are exposed

to higher stress, which has to be considered in the context of blend electrodes. In contrast, due to the minor volume fraction of SiO_x in the electrode, the blend design is expected to be beneficial in terms of buffering the total expansion of the SiO_x particles, resulting in reduced total electrode swelling in comparison to pure Si or SiO_x electrodes.

To further elucidate possible stress indicators on the particle level, the corresponding temporal expansion gradient—defined as the relative volume change per time interval ($\frac{\Delta V}{\Delta t}$)—is shown in Figure 7c,d for the separator and current collector interface, respectively.

Analogous to the impact of the strain rate in the discipline of mechanics, where a faster change in expansion can cause a switch from ductile to brittle behavior of a material,^[73] a faster change in volume is supposed to be detrimental for the AM particles. Hence, this could pose another risk for accelerated aging. The separator-facing particle is exposed to a peak expansion gradient of more than double the value at the CC (cf. Figure 7c,d). This indicates a slower and more homogeneous expansion near the CC, while a significantly increased mechanical stress generation is expected near the separator. During the C/3 lithiation process, each discrete particle shell displays a single, pronounced peak in gradient, while the gradient remains relatively low both before and after this peak. This peak occurs later at the particle center than at the surface but reaches a magnitude at least as high as the peak gradient at the surface. In the particles close to the separator, the peak gradient in the center of the particle even exceeds the gradient at the surface (cf. Figure 7c). Consequently, particles undergo high mechanical stress multiple times throughout electrode lithiation, as the DOL—and thus the volume expansion—propagates time-delayed from the surface to the center.

According to the literature, the inhomogeneous expansion of particle surface and center, caused by limited solid-state transport, increases the risk of particle fracturing, regardless of the material considered.^[9,66,74] Given that these inhomogeneities become more pronounced at higher intercalation currents, the fluctuating current split observed in the Gr/SiO_x electrode is expected to exacerbate this issue further. As demonstrated by using multiphysics models, particle fracturing and damage are enhanced during (de-)lithiation at higher C-rates.^[75,76] To mitigate expansion gradients, tailored design strategies, such as utilizing nanoscale particle sizes or porous particles, could be advantageous, as these approaches would result in shorter diffusion paths.^[18]

Additionally, the proportion of the two materials in the blend is a critical parameter that must be considered to reduce inhomogeneities, as demonstrated in simulation studies by Kespe et al.^[9] and Ai et al.^[27] who explored various virtual designs of an NMC/LMO blend cathode and a Si/Gr blend anode, respectively. Such tuning could also help to minimize mechanical stress generation due to a more homogeneous lithiation of the particles.

3.2.4. Comparison to Pure Gr Electrode

Furthermore, the effects of a blend electrode design on the considered stress indicators are evaluated through a comparison

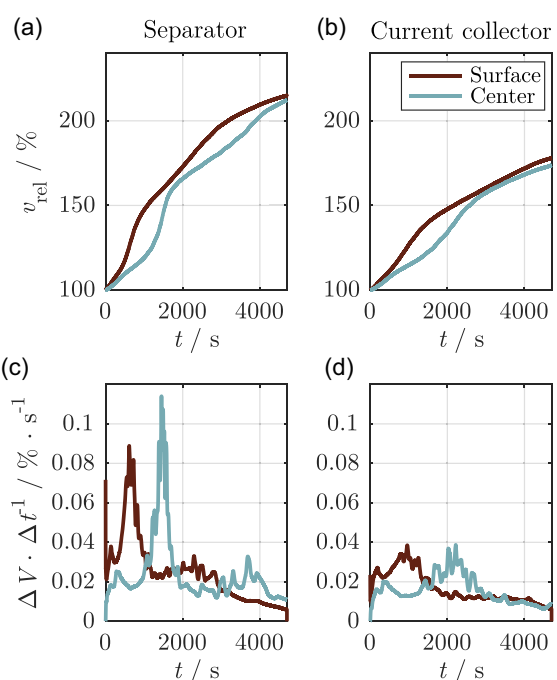


Figure 7. a,b) Relative volume and c,d) volume expansion gradient of SiO_x species during C/3 lithiation, calculated based on the local DOLs. The illustrations represent the particle surface and center, distinguishing between (a,c) the separator interface and (b,d) the CC interface.

between the Gr/SiO_x blend electrode and a pure Gr electrode. Therefore, the parameters of the Gr species contained in the blend are incorporated into the standard TLM. This enables a comparative analysis of the same material in two configurations under the conjecture that similar Gr material can be applied to both blend and pure electrode designs. Apart from that, the same average ionic resistance R_{ion} is allocated to the pure electrode to account for comparable microstructure properties. However, a constant value of R_{ion} is applied across the entire DOL range, as minimal volume expansion—and thus negligible change in porosity and ionic tortuosity—is expected. This contrasts with the SiO_x-containing blend, where a linear increase in R_{ion} with DOL is assumed (cf. Section 2.3). Following the described parameterization approach, the two modeled electrodes are deemed suitable for comparison with regard to their electrochemical behavior under load.

The primary advantage of incorporating Si or SiO_x into a Gr anode is the increased specific capacity, and thus, energy density. However, since these metrics are not the focus of the present work, we do not analyze capacity nor energy effects in this comparison. Instead, we concentrate on stress indicators and local states during operation.

For the analysis, constant-current lithiation of the pure Gr electrode is simulated at five different C-rates, analogous to the blend electrode, as shown in the previous sections. Since particles adjacent to the separator experience the highest peak intercalation currents, Figure 8a,b illustrates the local intercalation C-rate at the separator-facing electrode segment during lithiation at C/20 and C/3, respectively. The results are displayed until U_{cutoff} is reached in the blend electrode simulation. In the case of the blend electrode, the local C-rate is shown separately for the Gr and SiO_x fractions.

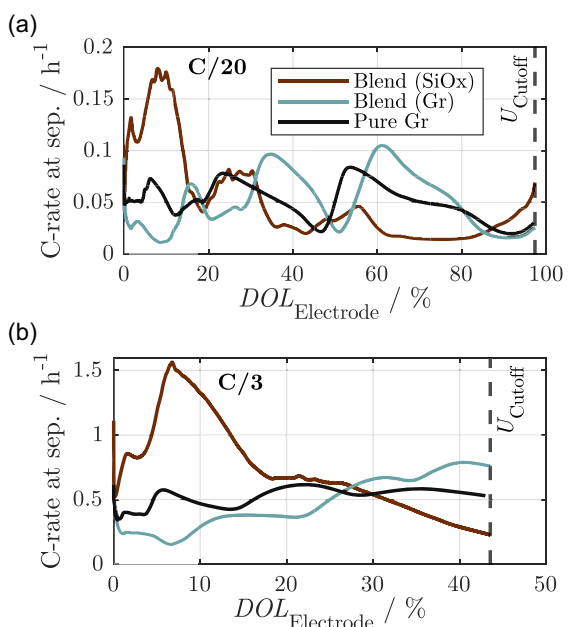


Figure 8. Comparison between Gr/SiO_x blend and pure Gr electrodes. Local C-rate at separator interface during constant-current lithiation with a) C/20 and b) C/3. The dotted vertical line represents the termination of the lithiation process of the blend electrode due to the terminal voltage falling below U_{cutoff} .

For both C-rates, the pure Gr electrode exhibits a smoother and a more stable course, whereas, the Gr and the SiO_x fractions in the blend electrode experience substantial fluctuations. As discussed previously, the blended design results in high SiO_x peaks at the beginning of lithiation, with Gr peaks becoming more pronounced at higher DOL (cf. Section 3.2.1). In comparison to the pure Gr electrode, even the peak C-rates of the Gr fraction in the blend are observed to be higher, while the minima are noted to be lower at both C/20 and C/3. Consequently, the lithiation process of the pure electrode is evidenced to be more homogeneous and uniform, despite the application of a similar global C-rate. Nevertheless, even in the pure Gr electrode, the particles at the separator are exposed to local peak C-rates that significantly exceed the global C-rate, which is evoked by the limited ionic transport in the porous electrode. In addition to these effects of limited transport, the differing OCP curves of Gr and SiO_x (cf. Figure 1c) within the blend electrode give rise to additional intensification of inhomogeneity during lithiation, with higher C-rate peaks compared to the pure electrode, where all particles display identical OCP characteristics.

To gain a comprehensive understanding, the results of all five C-rates are presented collectively in the Table S2, Supporting Information. The highest local C-rates in each material and the maximum observed DOL inhomogeneity (inter-particle and intra-particle) occurring during the lithiation process are compared. It should be noted that the simulation is terminated when $U_{\text{Electrode}}$ drops below U_{cutoff} . Consequently, the full DOL range cannot be utilized, particularly at higher C-rates (cf. Figure 3). This means that, for instance, regions where peak C-rates of Gr would typically appear in the blend are not reached at 1C and C/3. As a result, at 1C, the observed peak C-rate of Gr is higher in the pure electrode than in the blend since Gr experiences minimal utilization in the accessible region of the blend electrode. At all other evaluated C-rates, however, the maximum C-rate in the pure electrode remains lower than that in the Gr fraction of the blend. For instance, at C/3, a peak local C-rate of 0.79C arises in the Gr fraction in the blend compared to 0.63C in the pure electrode. Additionally, the maximum observable DOL inhomogeneity is reduced in the pure electrode across all C-rates below 1C, which is evident in both inter-particle and intra-particle inhomogeneity.

Apart from the inhomogeneity effects introduced by the blend design, similar trends are observed in the pure electrode when examining the influence of the C-rate. From C/40 to C/3, inter- and intra-particle DOL inhomogeneities increase at higher C-rates due to limitations in charge transport across the electrode thickness and within the particles. In the blend electrode, these effects are even more pronounced, with the Gr fraction experiencing higher peak C-rates compared to the pure electrode during constant-current lithiation. This trend holds for all but the highest evaluated C-rate (1C), where the SiO_x fraction primarily carries the applied current, and Gr is relatively inactive since the simulation is terminated at an early stage due to the cutoff voltage.

The findings suggest that a Gr/SiO_x blend electrode design may lead to an increase of the evaluated stress indicators in the Gr fraction, particularly when the DOL range in which Gr is active is fully utilized. The local intercalation current remains

more stable in the pure Gr electrode with reduced peak intensities. Conversely, the Gr fraction in the blend is spared if only the low DOL range is used where SiO_x is primarily active. This again highlights the nontrivial effects arising from blended designs. An optimized electrode design may be found depending on the specific use case and targeted by tailoring the ratio of the two species, as previously shown in model-based studies with varying amounts of the contained materials.^[9,27] Therefore, the presented model approach provides a valuable tool for future studies in the context of design optimization.

4. Conclusion

In this study, we presented a modeling approach for blend electrodes, which was applied to an anode containing graphite and silicon oxide. A spatially resolved TLM was adapted to simulate the electrochemical behavior of electrodes with two active materials in time domain. The TLM considers the main kinetic limitations emerging in porous electrodes as well as the OCP of the materials.

The model successfully reproduces key effects of the blend electrode, including the terminal voltage and the current split, validated against experimental data from a Gr/SiO_x model-like blend setup gained in a prior study.^[53] Simulating constant-current lithiation at varying C-rates (C/40 to 1C) revealed that the model qualitatively captured the experimentally observed current split between Gr and SiO_x. The TLM approach offers significant advantages over physics-based models, including fewer required parameters, lower computational cost, and straightforward parameterization based on impedance data and OCP curves. Despite its simplicity, the model offers spatial resolution in two dimensions, similar to conventional p2D models, thereby facilitating an examination of local states during operation.

Based on the simulation results, internal states were analyzed with regard to possible factors that could trigger detrimental effects and accelerate electrode degradation, referred to as stress indicators. In particular, the analysis focused on evaluating inhomogeneities in local material-specific current rates, local DOL, and volume expansion, as these factors can contribute to mechanical and electrochemical degradation. Valuable insights on the fluctuating intercalation C-rates exposed to the particles across the electrode thickness could be revealed, thereby distinguishing between the two active material species. Key findings highlight the amplified inhomogeneities in local C-rate and DOL in Gr/SiO_x blends, mainly driven by differences in OCP characteristics. For comparison, a pure Gr electrode was simulated with parameters identical to the Gr fraction of the blend electrode, showing fewer fluctuations in local C-rates. Inhomogeneity effects in the blend were particularly pronounced at medium and high C-rates; for example, during C/3 lithiation, SiO_x particles near the separator experienced local C-rates as high as 1.5C, exacerbating spatial DOL gradients due to kinetic limitations. Consequently, the model predicted significant gradients in volume expansion, with severe inhomogeneities inside the particles near the separator and relatively uniform behavior near the current collector.

This work underscores the utility of the TLM approach for understanding electrochemical phenomena in blend electrodes, providing valuable insights into the complex interplay of material-specific behavior and operational conditions, and laying the groundwork for future applications in blend electrode design optimization. A topic worth exploring in future research is the simulation-based investigation of the effects of varying AM proportions, requiring modified effective model parameters.

While this study focused on a Gr/SiO_x electrode, the approach is adaptable to various blend chemistries, provided sufficient data for parameterization is available. To expand its applicability, future studies should explore dynamic current profiles and validate the model with actual blend electrodes to confirm its effectiveness beyond the model-like setup used here. Experimental ageing studies could also be conducted to verify that the observed stress indicators correspond to increased electrode degradation. Additionally, incorporating current-dependent CT kinetics according to the Butler–Volmer equation could improve accuracy, particularly at higher C-rates, and will be a focus of future development.

Acknowledgements

The authors gratefully acknowledge Diego Knauer for his contribution to drafting the literature review for the introduction and for engaging in insightful discussions on the modeling approach. The authors would like to thank the German Federal Ministry of Education and Research (BMBF) within the framework of the FestBatt2 cluster (BMBF grant no. 03XP0441A).

Open Access funding enabled and organized by Projekt DEAL.

Conflict of Interest

The authors declare no conflict of interest.

Data Availability Statement

The simulation data presented in this work are available upon reasonable request.

Keywords: blend electrode • inhomogeneities • lithium-ion battery • stress • transmission line model

- [1] P. Albertus, S. Babinec, S. Litzelman, A. Newman, *Nat. Energy* **2018**, *3*, 16.
- [2] A. Manthiram, *Nat. Commun.* **2020**, *11*, 1550.
- [3] J. Baars, T. Domenech, R. Bleischwitz, H. E. Melin, O. Heidrich, *Nat. Sustainability* **2021**, *4*, 71.
- [4] A. W. Schäfer, S. R. H. Barrett, K. Doyme, L. M. Dray, A. R. Gnadt, R. Self, A. O'Sullivan, A. P. Synodinos, A. J. Torija, *Nat. Energy* **2019**, *4*, 160.
- [5] X.-G. Yang, T. Liu, S. Ge, E. Rountree, C.-Y. Wang, *Joule* **2021**, *5*, 1644.
- [6] C. Heubner, T. Liebmann, C. Lämmel, M. Schneider, A. Michaelis, *ChemElectroChem* **2018**, *5*, 425.
- [7] M. Casas-Cabanas, A. Ponrouch, M. R. Palacín, *Isr. J. Chem.* **2021**, *61*, 26.
- [8] S. B. Chikkannanavar, D. M. Bernardi, L. Liu, *J. Power Sources* **2014**, *248*, 91.
- [9] M. Kespe, S. Cernak, M. Gleiß, S. Hammerich, H. Nirschl, *Int. J. Energy Res.* **2019**, *248*, 91.
- [10] D. Wu, H. Ren, Y. Guo, X. Zhang, Z. Zhang, J. Li, *Ionics* **2019**, *25*, 1595.

- [11] S. Chae, S.-H. Choi, N. Kim, J. Sung, J. Cho, *Angew. Chem., Int. Ed. Engl.* **2020**, *59*, 110.
- [12] L. Gottschalk, C. Oertel, N. Strzelczyk, J. Müller, J. Krüger, W. Haselrieder, A. Kwade, *Energy Technol.* **2023**, *11*, A1598.
- [13] T. Placke, R. Kloepsch, S. Dühnen, M. Winter, *J. Solid State Electrochem.* **2017**, *21*, 1939.
- [14] J. Müller, M. Abdollahifar, A. Vinograd, M. Nöske, C. Nowak, S.-J. Chang, T. Placke, W. Haselrieder, M. Winter, A. Kwade, N.-L. Wu, *Chem. Eng. J.* **2021**, *407*, 126603.
- [15] M. Wetjen, D. Pritzl, R. Jung, S. Solchenbach, R. Ghadimi, H. A. Gasteiger, *J. Electrochem. Soc.* **2017**, *164*, A2840.
- [16] F. Jeschull, Y. Surace, S. Zürcher, M. E. Spahr, P. Novák, S. Trabesinger, *Electrochim. Acta* **2019**, *320*, 134602.
- [17] Y. Jin, B. Zhu, Z. Lu, N. Liu, J. Zhu, *Adv. Energy Mater.* **2017**, *7*, 1700715.
- [18] M. Jiao, Y. Wang, C. Ye, C. Wang, W. Zhang, C. Liang, *J. Alloys Compd.* **2020**, *842*, 155774.
- [19] D. Chatzogiannakis, V. Arszelewska, P.-E. Cabelguen, F. Fauth, M. Casas-Cabanas, M. R. Palacin, *Energy Storage Mater.* **2024**, *69*, 103414.
- [20] T. Liebmam, C. Heubner, M. Schneider, A. Michaelis, *Mater. Today Energy* **2021**, *22*, 100845.
- [21] M. Doyle, T. F. Fuller, J. Newman, *J. Electrochem. Soc.* **1993**, *140*, 1526.
- [22] M. Doyle, J. P. Meyers, J. Newman, *J. Electrochem. Soc.* **2000**, *147*, 99.
- [23] T. F. Fuller, M. Doyle, J. Newman, *J. Electrochem. Soc.* **1994**, *141*, 1, https://doi.org/10.1149/1.2054684.
- [24] A. Rodríguez, G. L. Plett, *J. Energy Storage* **2017**, *11*, 219.
- [25] O. von Kessel, T. Hoehl, P. Heugel, F. Brauchle, D. Vrankovic, K. P. Birke, *J. Electrochem. Soc.* **2023**, *170*, 090534.
- [26] J. Sturm, A. Rheinfeld, I. Zilberman, F. B. Spingler, S. Kosch, F. Frie, A. Jossen, *J. Power Sources* **2019**, *412*, 204.
- [27] W. Ai, N. Kirkaldy, Y. Jiang, G. Offer, H. Wang, B. Wu, *J. Power Sources* **2022**, *527*, 231142.
- [28] D. J. Pereira, A. M. Aleman, J. W. Weidner, T. R. Garrick, *J. Electrochem. Soc.* **2022**, *169*, 020577.
- [29] P.-F. Lory, B. Mathieu, S. Genies, Y. Reynier, A. Boulineau, W. Hong, M. Chandresris, *J. Electrochem. Soc.* **2020**, *167*, 120506.
- [30] P. Albertus, J. Christensen, J. Newman, *J. Electrochem. Soc.* **2009**, *156*, A606.
- [31] Z. Chen, D. L. Danilov, Q. Zhang, M. Jiang, J. Zhou, R.-A. Eichel, P. H. Notten, *Electrochim. Acta* **2022**, *430*, 141077.
- [32] X. Zhang, J. Chen, Y. Bao, *Energies* **2022**, *15*, 8848.
- [33] Q. Liang, M. Z. Bazant, *J. Electrochem. Soc.* **2023**, *170*, 093510.
- [34] L. Boveleth, A. Lindner, W. Meneskou, T. Danner, A. Latz, *Electrochim. Acta* **2024**, *506*, 145010.
- [35] J. Le Houx, D. Kramer, *Energy Rep.* **2020**, *6*, 1, https://doi.org/10.1016/j.egyr.2020.02.021.
- [36] A. A. Wang, S. E. J. O’Kane, F. B. Planella, J. Le Houx, K. O’Regan, M. Zyskin, J. Edge, C. W. Monroe, S. J. Cooper, D. A. Howey, E. Kendrick, J. M. Foster, *Prog. Energy.* **2021**, *4*, 32004.
- [37] D. Beck, M. Dubarry, *Batteries* **2024**, *10*, 159.
- [38] M. Dubarry, D. Beck, *Acc. Mater. Res.* **2022**, *3*, 843.
- [39] J. Costard, *Einfluss von Mikrostruktur und Materialparametern auf die Leistungsfähigkeit poröser Elektroden für Lithium-Ionen Batterien*, Schriften des Instituts für Angewandte Materialien - Werkstoffe der Elektrotechnik, Karlsruher Institut für Technologie/Institut für Angewandte Materialien - Werkstoffe der Elektrotechnik, KIT Scientific Publishing, Karlsruhe, Germany **2018**, https://doi.org/10.1016/C2013-0-06263-9.
- [40] J. Landesfeind, J. Hattendorff, A. Ehrl, W. A. Wall, H. A. Gasteiger, *J. Electrochem. Soc.* **2016**, *163*, A1373.
- [41] J. Jamnik, J. Maier, S. Pejovnik, *Electrochim. Acta* **1999**, *44*, 4139.
- [42] R. de Levie, *Electrochim. Acta* **1963**, *8*, 751.
- [43] S. D. Talian, S. Brutt, M. A. Navarra, J. Moškon, M. Gaberscak, *Energy Storage Mater.* **2024**, *69*, 103413.
- [44] N. Togasaki, A. Nakao, T. Tanaka, U. Harada, H. Onish, H. Yasuda, S. Kobayashi, F. Maeda, T. Osaka, *J. Electrochem. Soc.* **2023**, *170*, 050519.
- [45] V. Miß, A. Ramanayagam, B. Roling, *ACS Appl. Mater. Interfaces* **2022**, *14*, 38246.
- [46] S. Drvarić Talian, J. Bobnar, A. R. Sinigoj, I. Humar, M. Gaberšček, *J. Phys. Chem. C* **2019**, *123*, 27997.
- [47] T. A. Hendriks, M. A. Lange, E. M. Kiens, C. Baeumer, W. G. Zeier, *Batteries Supercaps* **2023**, *6*, e202200544.
- [48] P. Minnmann, L. Quillman, S. Burkhardt, F. H. Richter, J. Janek, *J. Electrochem. Soc.* **2021**, *168*, 040537.
- [49] M. Hahn, A. Schiela, P. Mößle, F. Katzer, M. A. Danzer, *J. Power Sources* **2020**, *477*, 228672.
- [50] M. Hahn, L. Grüne, C. Plank, F. Katzer, T. Rüther, L. Jahn, M. A. Danzer, *J. Energy Storage* **2021**, *42*, 103056.
- [51] G. L. Plett, M. S. Trimble, in *2024 Int. Conf. on Electrical, Computer and Energy Technologies (ICECET)*, IEEE, Sydney, Australia, July **2024**, pp. 1–6, https://doi.org/10.1109/ICECET61485.2024.10698098.
- [52] Z. Chen, D. L. Danilov, R.-A. Eichel, P. H. L. Notten, *Adv Energy Mater.* **2022**, *12*, 170179.
- [53] J. Knorr, J. Li, M. Schamel, T. Kufner, A. Adam, M. A. Danzer, *J. Electrochem. Soc.* **2024**, *171*, 080512.
- [54] G. L. Plett, *J. Power Sources* **2004**, *134*, 262.
- [55] F. Baronti, N. Femia, R. Saletti, C. Visone, W. Zamboni, *J. Energy Storage* **2015**, *4*, 51.
- [56] C. Guenther, J. K. Barillas, S. Stumpp, M. A. Danzer, in *2012 3rd IEEE PES Innovative Smart Grid Technologies Europe (ISGT Europe)*, IEEE, Berlin, Germany October **2012**, pp. 1–7, https://doi.org/10.1109/ISGTEurope.2012.6465855.
- [57] L. Jahn, P. Mößle, F. Röder, M. A. Danzer, *Commun. Eng.* **2024**, *3*, 321.
- [58] J. Schmitt, I. Horstkötter, B. Bäker, *J. Power Sources* **2024**, *26*, 100139.
- [59] D. Wycisk, M. Oldenburger, M. G. Stoye, T. Mrkonjic, A. Latz, *J. Energy Storage* **2022**, *52*, 105016.
- [60] C. Heubner, T. Liebmam, O. Lohrberg, S. Cangaz, S. Maletti, A. Michaelis, *Batteries Supercaps* **2022**, *5*, e202100182.
- [61] T. Liebmam, C. Heubner, C. Lämmel, M. Schneider, A. Michaelis, *ChemElectroChem* **2019**, *6*, 5728.
- [62] H. Seyle, *Stress in Health and Disease*, Elsevier **1976**.
- [63] J. Kim, W. Lee, J. Seok, S. Park, J. K. Yoon, S.-B. Yoon, W.-S. Yoon, *Cell Rep. Phys. Sci.* **2023**, *4*, 101331.
- [64] Y. Qi, T. Jang, V. Ramadesigan, D. T. Schwartz, V. R. Subramanian, *J. Electrochem. Soc.* **2017**, *164*, A3196.
- [65] L. Kraft, J. B. Habedank, A. Frank, A. Rheinfeld, A. Jossen, *J. Electrochem. Soc.* **2020**, *167*, 013506.
- [66] E. Bohn, T. Eckl, M. Kamlah, R. McMeeking, *J. Electrochem. Soc.* **2013**, *160*, A1638.
- [67] J. Vetter, P. Novák, M. R. Wagner, C. Veit, K.-C. Möller, J. O. Besenhard, M. Winter, M. Wohlfahrt-Mehrens, C. Vogler, A. Hammouche, *J. Power Sources* **2005**, *147*, 269.
- [68] M. Ashuri, Q. He, L. L. Shaw, *Nanoscale* **2016**, *8*, 74.
- [69] C. Liu, O. Arcelus, T. Lombardo, H. Oularbi, A. A. Franco, *J. Power Sources* **2021**, *512*, 230486.
- [70] F. Silveri, M. Alberghini, V. Esnault, A. Bertinetti, V. Rouchon, M. Giuliano, G. Gudendorff, C. Zhao, J. Bikard, M. Sgroi, A. Tommasi, M. Petit, *J. Power Sources* **2024**, *598*, 234109.
- [71] A. J. Louli, J. Li, S. Trussler, C. R. Fell, J. R. Dahn, *J. Electrochem. Soc.* **2017**, *164*, A2689.
- [72] S. C. Jung, H.-J. Kim, J.-H. Kim, Y.-K. Han, *J. Phys. Chem. C* **2016**, *120*, 886.
- [73] D. R. Askeland, W. J. Wright, *The Science and Engineering of Materials*, SI Edition, 7th ed., Cengage Learning, Boston, MA **2016**.
- [74] Z. Zeng, N. Liu, Q. Zeng, S. W. Lee, W. L. Mao, Y. Cui, *Nano Energy* **2016**, *22*, 105.
- [75] H. Tian, L. T. Gao, Z.-S. Guo, *J. Electrochem. Soc.* **2022**, *169*, 090513.
- [76] W. Ai, B. Wu, E. Martínez-Pañeda, *J. Power Sources* **2022**, *544*, 231805.

Manuscript received: February 28, 2025

Revised manuscript received: April 14, 2025

Version of record online: